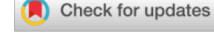
RESEARCH ARTICLE



MEDICAL PHYSICS

Rapid CNN-based needle localization for automatic slice alignment in MR-guided interventions using 3D undersampled radial white-marker imaging

Jonas Frederik Faust^{1,2} | Axel Joachim Krafft² | Daniel Polak² | Peter Speier² | Nicolas Gerhard Roland Behl² | Nathan Ooms^{3,4} | Jesse Roll³ | Joshua Krieger³ | Mark Edward Ladd^{1,5,6} | Florian Maier²

Correspondence

Jonas Frederik Faust, Siemens Healthineers AG, Allee am Röthelheimpark 2, 91052 Erlangen, Germany. Email:

jonas.faust@siemens-healthineers.com

Abstract

Background: In MR-guided in-bore percutaneous needle interventions, typically 2D interactive real-time imaging is used for navigating the needle into the target. Misaligned 2D imaging planes can result in losing visibility of the needle in the 2D images, which impedes successful targeting. Necessary iterative manual slice adjustment can prolong interventional workflows. Therefore, rapid automatic alignment of the imaging planes with the needle would be preferable to improve such workflows.

Purpose: To investigate rapid 3D localization of needles in MR-guided interventions via a convolutional neural network (CNN)-based localization algorithm using an undersampled white-marker contrast acquisition for the purpose of automatic imaging slice alignment.

Methods: A radial 3D rf-spoiled gradient echo MR pulse sequence with white-marker encoding was implemented and a CNN-based localization algorithm was employed to extract position and orientation of an aspiration needle from the undersampled white-marker images. The CNN was trained using porcine tissue phantoms (257 needle trajectories, four-fold data augmentation, 90%/10% split into training and validation dataset). Achievable localization times and accuracy were evaluated retrospectively in an ex vivo study (109 needle trajectories) for a range of needle orientations between 78° and 90° relative to the B_0 field. A proof-of-concept in vivo experiment was performed in two porcine animal models and feasibility of automatic imaging slice alignment was evaluated retrospectively.

Results: Ex vivo needle localization was achieved with a median localization accuracy of 1.9 mm (distance needle tip to detected needle axis) and a median angular deviation of 2.6° for needle orientations between 86° and 90° to the B_0 field from fully sampled WM images (resolution of $(4 \text{ mm})^3$, 6434 acquired radial k-space spokes, acquisition time of 80.4 s) in a field-of-view of $(256 \text{ mm})^3$. Localization accuracy decreased with increasing undersampling and needle trajectory increasingly aligned with B_0 . For needle orientations between 86° and 90° to the B_0 field, a highly accelerated acquisition of only 32 k-space spokes (acquisition time of 0.4 s) yielded a median localization accuracy of 3.1 mm

188 wileyonlinelibrary.com/journal/mp Med Phys. 2024;51:8018–8033.

¹Faculty of Physics and Astronomy, Ruprecht-Karls-Universität Heidelberg, Heidelberg, Germany

²Siemens Healthineers AG, Erlangen, Germany

³Cook Advanced Technologies, West Lafayette, Indiana, USA

⁴School of Health Sciences, Purdue University, West Lafayette, Indiana, USA

Medical Physics in Radiology, German Cancer Research Center (DKFZ), Heidelberg, Germany

⁶Faculty of Medicine, Ruprecht-Karls-Universität Heidelberg, Heidelberg, Germany

This is an open access article under the terms of the Creative Commons Attribution License, which permits use, distribution and reproduction in any medium, provided the original work is properly cited.

^{© 2024} Siemens Healthineers AG, Cook Advanced Technologies and The Author(s). *Medical Physics* published by Wiley Periodicals LLC on behalf of American Association of Physicists in Medicine.

and a median angular deviation of 4.7° . For needle orientations between 78° and 82° to the B_0 field, a median accuracy and angular deviation of 3.5 mm and 6.8° could still be achieved with 64 sampled spokes (acquisition time of 0.8 s). In vivo, a localization accuracy of 1.4 mm and angular deviation of 3.4° was achieved sampling 32 k-space spokes (acquisition time of 0.48 s) with the needle oriented at 87.7° to the B_0 field. For a needle oriented at 87.7° to the 80 field, localization accuracy of 80 mm and angular deviation of 80 were still achieved sampling 800 k-space spokes (acquisition time of 800 kg were still achieved sampling 801 k-space spokes (acquisition time of 801 kg were still achieved sampling 801 k-space spokes (acquisition time of 801 kg were still achieved sampling 801 k-space spokes (acquisition time of 801 kg were still achieved sampling 801 k-space spokes (acquisition time of 801 kg were still achieved sampling 802 k-space spokes (acquisition time of 802 kg were still achieved sampling 803 k-space spokes (acquisition time of 803 kg were still achieved sampling 803 k-space spokes (acquisition time of 803 kg were still achieved sampling 803 kg were still ach

Conclusion: The investigated approach enables passive biopsy needle localization in 3D. Acceleration of the localization to real-time applicability is feasible for needle orientations approximately perpendicular to B_0 . The method can potentially facilitate MR-guided needle interventions by enabling automatic imaging slice alignment with the needle.

KEYWORDS

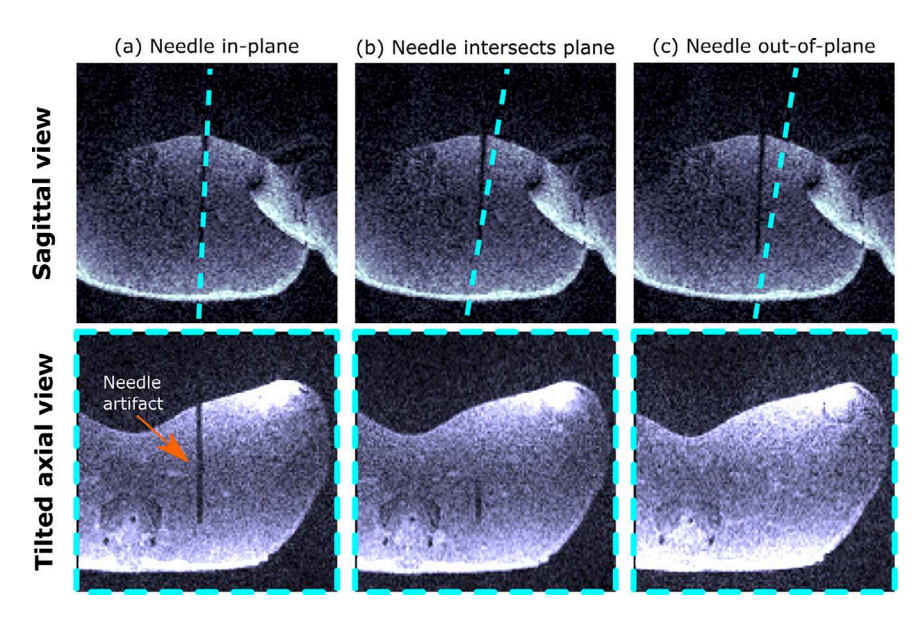
device localization, interventional MRI, percutaneous needle intervention

1 | INTRODUCTION

Percutaneous needle interventions are commonly performed minimally invasive procedures for diagnostic or therapeutic purposes. 1,2 To enable targeting of small lesions, image guidance is employed. Compared to other imaging modalities, such as computed tomography (CT) or ultrasound (US), MRI provides excellent soft tissue contrast and the ability for functional measurements. In contrast to CT, it does not expose the interventionalist and the patient to ionizing radiation. Despite these advantages, MR guidance for percutaneous needle interventions has not yet been adopted for broad clinical use. One major limitation are complex workflows, often including time-consuming manual imaging slice adjustment to align 2D real-time imaging planes with the needle for appropriate guidance. Figure 1 illustrates how potential misalignments of a 2D imaging plane with a needle determines device visibility.

To simplify and accelerate workflows for MR-guided percutaneous needle interventions and therefore allow for an easier adoption into clinical practice, techniques for computer-assisted needle localization have been developed. So-called passive tracking techniques leverage the MR image artifact introduced by the device itself for localization. The magnetic susceptibility of metallic devices can cause signal dephasing in the surrounding tissue due to locally induced field gradients from which the device position can be inferred.⁴ Seppenwoolde et al. introduced so-called white-marker (WM) imaging⁵ to generate a positive susceptibility-based contrast for visualization of metallic devices. Additional magnetic field gradients are played out during spoiled gradient echo (GRE) image acquisition in a way that they partially refocus the dephased magnetization near the interventional device and therefore create a hyperintense device artifact on an otherwise partially or fully dephased background.

FIGURE 1 GRE images of needle placement in a pig's thigh with illustration of potential slice misalignment. The first row shows a sagittal plane including the needle. The second row shows a manually tilted axial plane, which (a) is fully aligned with the needle, (b) intersects with the needle, and (c) does not contain the needle. The placement of the tilted axial slice is indicated in the sagittal view by the blue dashed line. In in-bore needle interventions, (automatic) needle plane alignment will be necessary if the needle is not aligned with the chosen real-time imaging plane as shown in the illustration.



2473429, 2024, 11, Downloaded from https://alapm.onlinelibrary.wiely.com/doi/10.1002/mp.17376 by Dkfz Zentralbibliothek Krebsforschungszentrum, Wiley Online Library on [01/10/2025]. See the Terms and Conditions (https://onlinelibrary.wiely.com/terms-and-conditions) on Wiley Online Library for rules of use; O. Articles as governed by the applicable Creative Commons License

For passive needle localization, the use of convolutional neural networks (CNNs) has been proposed. Li et al. trained a CNN to detect the needle artifact in 2D spoiled GRE images of gel- and ex vivo tissue phantoms, as well as turbo spin echo images from prostate biopsies.⁶ Mehrtash et al. implemented a CNN to localize needle artifacts from 3D spin-echo images during prostate biopsies to characterize the needle tip position and the needle orientation in 3D space. Weine et al. implemented a CNN (U-Net architecture⁸) to localize needle artifacts in 2D images of liver biopsies, using spoiled GRE as well as WM contrast for the instrument localization.9

3D needle localization can help to facilitate the interventional procedure, e.g., by enabling automatic alignment of the imaging planes with the needle. Long image acquisition times, however, hamper the applicability of 3D image-based needle localization techniques in real-time procedures and alternative approaches have been proposed. De Oliveira et al. introduced a phaseonly cross correlation method making use of two parallel tracking slices to detect the position of a passive marker attached to a biopsy needle. 10 Reichert et al. extended the method introduced by Oliveira et al., reducing the acquisition time for the tracking slices by employing an undersampled radial acquisition. 11 The method requires prior knowledge of the needle's approximate orientation and location to correctly place the tracking slices. Patil et al. proposed a method to localize a paramagnetic marker that can be attached to interventional devices. 12 Using three echo-dephased projection acquisitions (comparable to WM contrast imaging), the position of the marker was determined in 3D space. The technique does, however, not allow an extraction of the orientation of the device, e.g., for an alignment of an imaging slice with a needle trajectory. Zijlstra et al. investigated a method where an undersampled radial acquisition of 2D WM images was used in combination with phase correlation template matching. 13 The tip of a titanium biopsy needle, which was inserted into ex vivo porcine phantoms, was tracked in two orthogonal slices. For this technique, the orientation of the needle is assumed to be known a priori, and tracking is not possible if the needle tip is not visible in at least one plane. Li et al. trained a CNN to determine the orientation and position of a needle across a slab of three 2D imaging slices, e.g., to correct for misalignment of the needle trajectory.¹⁴ This technique also requires prior knowledge about the approximate needle orientation and position to orient the slices.

In this work, we investigated a fully 3D image-based needle localization approach for the purpose of rapid automatic slice alignment during MR interventions without the need of prior information on needle position, employing a CNN-based localization algorithm to extract the position and orientation of a needle from undersampled 3D WM images. The CNN was trained using porcine tissue phantoms. The localization accuracy was evaluated and compared for different acceleration factors (applying retrospective undersampling) in an ex vivo study, as well as in a proof-of-concept in vivo experiment using two porcine animal models.

METHODS 2

Needle localization technique

For the proposed needle localization method, a research MR imaging sequence was implemented to acquire (undersampled) 3D WM images. Based on the WM images, the position and orientation of a needle were estimated using a CNN-based localization algorithm.

2.1.1 3D radial white-marker acquisition

A radial, rf-spoiled^{15,16} GRE-based WM 3D imaging sequence was implemented (Figure 2a). The implemented radial sampling scheme followed a 3D Golden Angle trajectory (Figure 2b), allowing for retrospective undersampling.¹⁷ To generate WM contrast, an additional gradient moment in z-direction (direction of B_0) was added to the sequence before the readout gradient. The WM gradient moment induces an additional phase to the magnetization, shifting the acquired k-space in zdirection by 2π . In areas with homogeneous magnetic field, the WM gradient moment dephases the magnetization and enforces signal suppression. As a metallic needle locally distorts the magnetic field, the locally induced gradient counteracts the WM gradient near the device and eventually restores signal in the vicinity of the needle (WM artifact). As the induced magnetic field distortion depends on the needle's orientation to the B₀ field, 18 the WM needle artifact also changes with the needle's orientation. Local susceptibility gradient compensation, and therefore WM signal, is maximized for a needle orientation orthogonal to the B₀ field and the WM gradient direction. WM signal is reduced for needle trajectories increasingly parallel to B₀, as demonstrated in Figure 2c.

To employ 3D WM imaging for needle localization, a CNN-based localization algorithm was implemented in Python. In Figure 3a, the steps of the developed image processing pipeline are illustrated for a representative needle placement in a porcine tissue phantom. In a first step, k-space data is acquired with the WM sequence. An image is reconstructed from the acquired k-space data using a Non-Uniform Fast Fourier Transform (NUFFT) procedure (density correction + gridding + FFT).²⁰ The reconstructed magnitude image is then processed by the CNN. A 3D U-Net architecture²¹ was

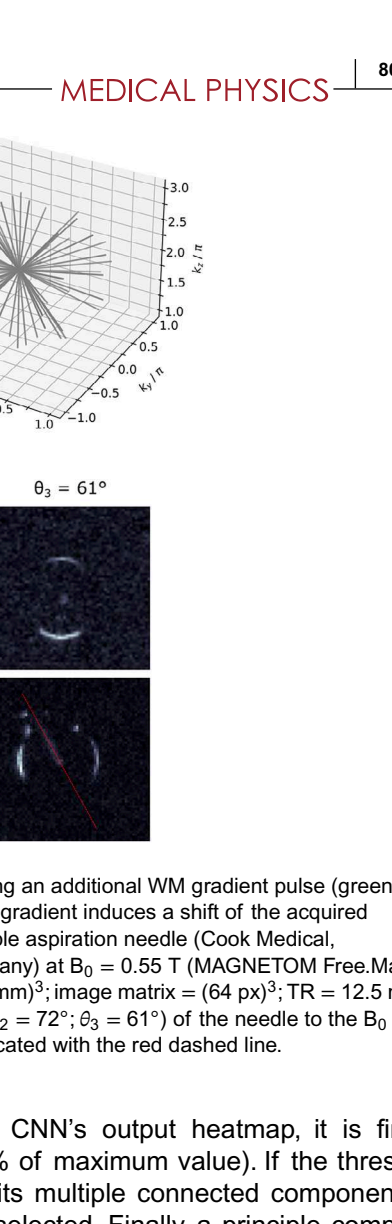


FIGURE 2 (a) Pulse diagram of implemented radial rf-spoiled spoiled GRE sequence, including an additional WM gradient pulse (green). (b) k-Space diagram showing 30 spokes of the radial readout trajectory of the sequence. The WM gradient induces a shift of the acquired k-space in k_z direction by 2π . (c) WM image acquisition demonstrated for a 22-gauge MR-compatible aspiration needle (Cook Medical, Bloomington, Indiana, USA) in a gel phantom (HVDE hydrogel, Schauch, Lauffen am Neckar, Germany) at $B_0 = 0.55$ T (MAGNETOM Free.Max, Siemens Healthineers AG, Erlangen, Germany) with the implemented WM sequence [FOV = $(256 \text{ mm})^3$; image matrix = $(64 \text{ px})^3$; TR = 12.5 ms; TE = 10 ms; flip angle = 10° ; bandwidth = 900 Hz/voxel] for different inclination angles ($\theta_1 = 90^\circ$; $\theta_2 = 72^\circ$; $\theta_3 = 61^\circ$) of the needle to the B_0 field. Tilting the phantom toward the direction of B_0 reduces the WM signal. The needle axis is indicated with the red dashed line.

 $\theta_1 = 90^{\circ}$

(b)

 $\theta_2 = 72^{\circ}$

implemented (Figure 3b) in Keras with the Tensorflow framework (Google Brain, Mountain View, California, USA). The network consists of a contracting path and an expansive path. In the contracting path, each step contains two $3 \times 3 \times 3$ convolutions (padded, stride of 1), each followed by a ReLU activation function, and a $2 \times 2 \times 2$ max pooling operation with a stride of 2 for downsampling. After the last downsampling step, again two $3 \times 3 \times 3$ convolutions (padded, stride of 1), each followed by a ReLU, are applied (bottleneck step) before the feature maps are fed into the expanding path. Here, each step consists of a $2 \times 2 \times 2$ upsampling with stride 1 and two 3 x 3 x 3 convolutions (padded, stride of 1), each followed by a ReLU. After each downsampling step, the number of feature channels is doubled. After each upsampling step, the number of feature channels is halved. Skip connections connect the different steps of the contracting path with the corresponding steps in the expanding path and concatenate the respective feature maps. In the final step, an additional convolution layer with linear activation reduces the number of feature maps to one. The network regresses from the input image toward the needle path, generating a heatmap with the same resolution as the input WM image, indicating the detected needle path. To determine the orientation of the nee-

ADC

(c)

dle path from the CNN's output heatmap, it is first thresholded (> 50% of maximum value). If the threshold heatmap exhibits multiple connected components, the largest one is selected. Finally, a principle component analysis (PCA) is performed, which has previously been proposed for determining object orientation in MR scans from CNN-based segmentation.²² The first principle axis is extracted and interpreted as the needle axis (passing through the centroid of the CNN heatmap). The implemeted model will be made public on GitHub post-publication.

2.2 | Localization study

The CNN was trained using porcine tissue phantoms and the proposed needle localization was evaluated in an ex vivo study, as well as in in vivo proof-of-concept experiments using two porcine animal models.

2.2.1 | Datasets

For the training of the CNN and the evaluation of the needle localization method, three datasets were

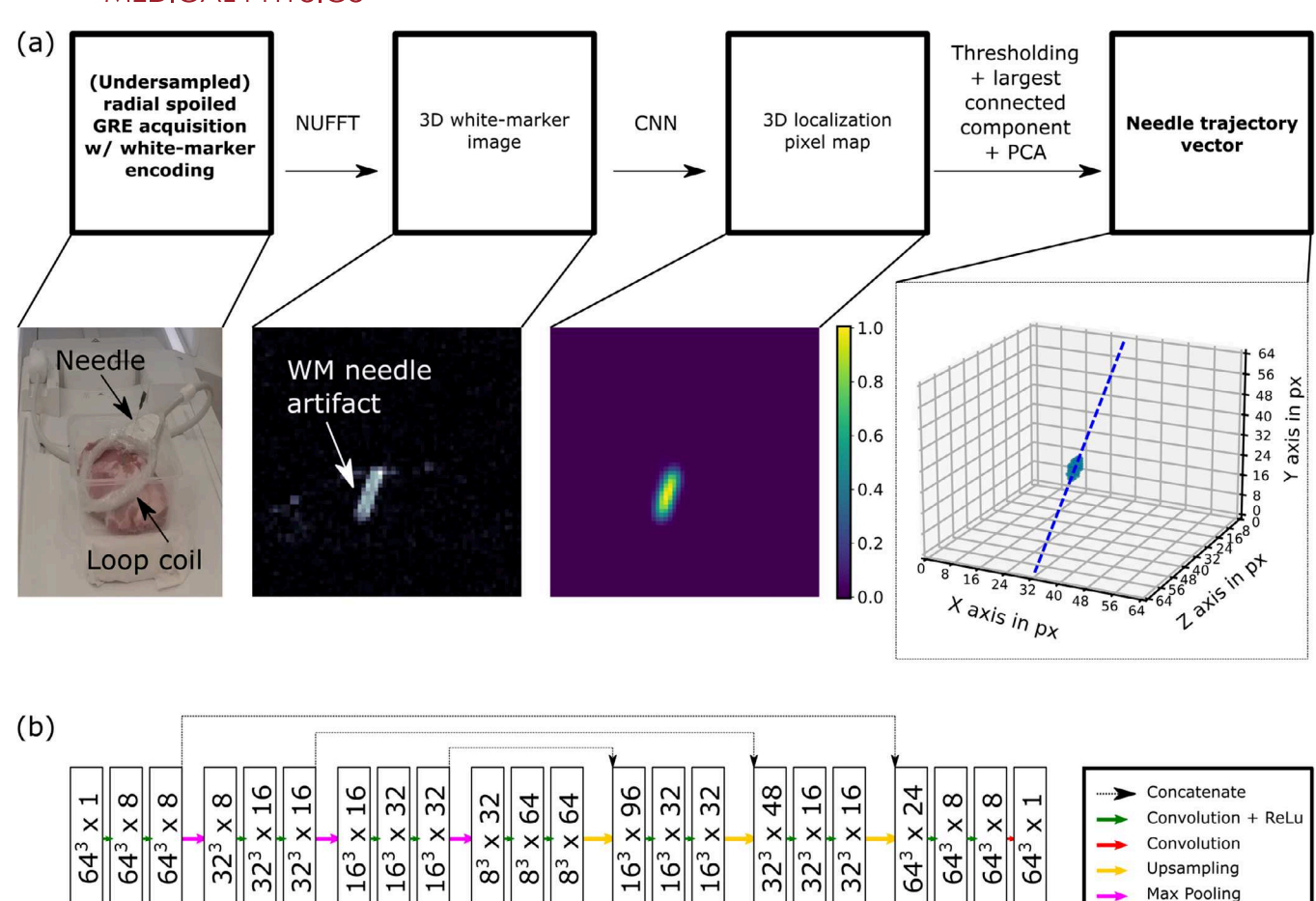


FIGURE 3 (a) Algorithm for 3D needle localization. The algorithm takes a WM acquisition as input, shown here for an ex vivo porcine tissue phantom with an aspiration needle. After image reconstruction using a NUFFT, the WM image is passed through a 3D CNN, which was trained to regress towards the needle path. A PCA is performed on the CNN's output heatmap (thresholded + largest connected component search), and the first principal axis is interpreted as the orientation of the needle axis. (b) 3D U-Net architecture of the implemented CNN. Volume images are passed through the net, undergoing multiple processing steps. Boxes show (image matrix x number of feature maps).

acquired (Table 1). All datasets were acquired at $B_0 = 0.55 \text{ T}$ (MAGNETOM Free.Max, Siemens Healthineers AG, Erlangen, Germany).

Training dataset

To train the CNN, a 22-gauge MR-compatible aspiration needle (Cook Medical, Bloomington, Indiana, USA) was inserted into seven porcine phantoms (muscle tissue, permeated with fatty tissue) and WM images were acquired for a total of 274 different needle trajectories (see description of training dataset in Table 1). Four-fold data augmentation was performed by randomly shifting the reconstructed FOV (ensuring that the entire needle path within the tissue was always visible in the shifted FOV). In addition to the acquisition of WM images, conventional rf-spoiled GRE images [FOV = $(256 \text{ mm})^3$; image matrix = $(128 \text{ px})^3$; TR = 4.5 ms; TE = 2.31 ms; flip angle = 6° ; bandwidth = 1600 Hz/pixel] were acquired of each new needle insertion to extract the ground truth needle path (Figure 4a). Entry and tip point of

the needle were manually annotated in the 3D GRE images and label images (Figure 4b) were generated by connecting the annotated entry and tip point with a straight line, blurred with a Gaussian filter (standard deviation = 6 mm). The phantoms were placed in a head coil for data acquisition as the set-up allowed for easy repositioning of the phantom without changing the coil configuration; for every needle trajectory, the phantom was rotated before reinserting the needle to increase variation in the data. Needle orientation was randomly sampled from a predefined angular range, characterized by the inclination angle θ of the needle with respect to the B_0 direction and the azimuthal angle φ of the needle trajectory, describing the angle that the needle encloses with the sagittal plane (Figure 4c). θ was sampled over a range of $\theta \in [73^{\circ}, 90^{\circ}]$, i.e., the needle was tilted out of the orthogonal to B₀ towards positive and negative z-direction. Simultaneously, φ was sampled over a range of $\varphi \in [0^{\circ}, 30^{\circ}]$ by tilting the needle out of the yz-plane towards positive and negative x-direction.

TABLE 1 Description of datasets (WM imaging sequence parameters and sampled needle trajectories) used for training of the CNN and in the ex vivo study, as well as in the in vivo proof-of-principle experiments.

	Ex vivo training set	Ex vivo test set	In vivo proof-of-principle experiments	
Number of phantoms/in vivo models	7	4	2	
Number of images	$\begin{array}{l} n_{total} = 257 \; (n_1 = 36, n_2 = 49, \\ n_3 = 36, n_4 = 40, n_5 = 19, n_6 = \\ 36, n_7 = 41); \\ n_{total\; (aug)} = 1028 \; \text{with four-fold} \\ \text{augmentation; split into} \\ \text{training/validation set: } 90\%/10\%) \end{array}$	$n_{total} = 109 (n_1 = 40, n_1 = 21, n_3 = 19, n_4 = 29)$	$n_{total} = 3 (n_1 = 1, n_2 = 2)$	
Needle type	22-gauge aspiration needle	22-gauge aspiration needle	20-gauge (animal 1) and 22-gauge aspiration needle (animal 2)	
Inclination (θ) Azimuthal angle (φ)	$\theta \in [73^{\circ}, 90^{\circ}]$ $\varphi \in [0^{\circ}, 30^{\circ}]$	$\theta \in [78^\circ, 90^\circ]$ $\varphi \in [0^\circ, 30^\circ]$	$\theta_1 = 87.7^\circ; \theta_2 = 88.8^\circ; \theta_3 = 77.6^\circ$ $\varphi_1 = 0.3^\circ; \varphi_2 = 15.7^\circ; \varphi_3 = 17.3^\circ$	
Insertion depth (I)	I ∈ {4 cm, 5 cm}	l ∈ {4 cm, 5 cm}	$I_1 = 11 \text{ cm}; I_2 = 8 \text{ cm}; I_3 = 8 \text{ cm}$	
Echo time (TE) Repetition time (TR)	TE = 10 ms TR = 12.5 ms	TE = 10 ms TR = 12.5 ms	TE = 10 ms TR = 15 ms	
Field of view	(256 cm) ³	$(256 \text{ cm})^3$	(256 cm) ³	
Resolution	(4 mm) ³	(4 mm) ³	(4 mm) ³	
Flip angle	10°	10°	10°	
Bandwidth	900 Hz/px	900 Hz/px	160 Hz/px	
Coil set-up	Head coil	Spine coil + loop coil	Spine coil + loop coil (animal 1 & / Spine coil + flex coil (animal 2)	

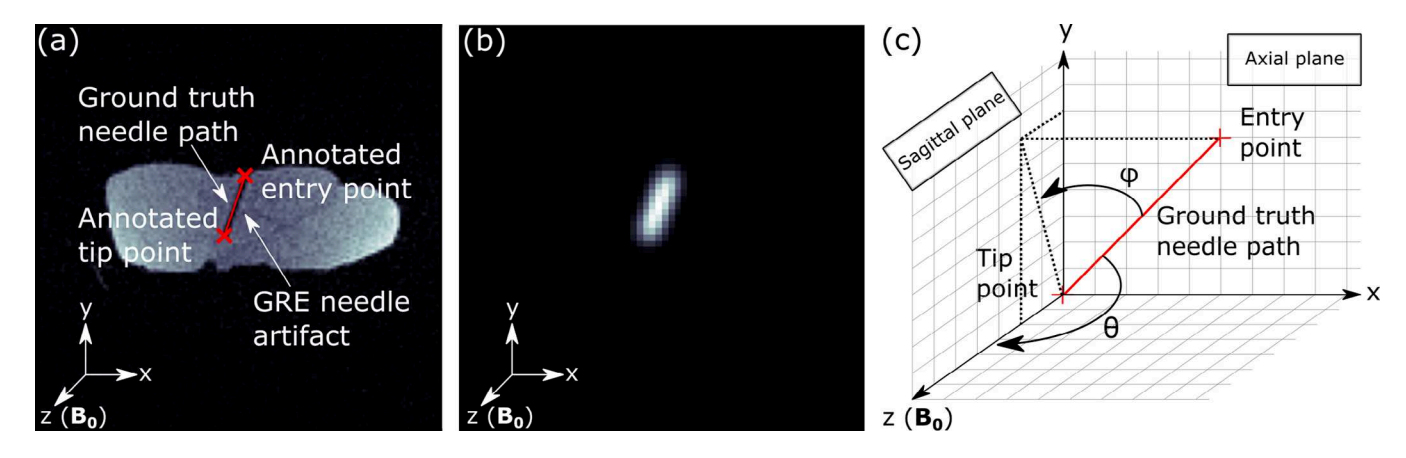


FIGURE 4 (a) Single slice of spoiled 3D GRE image of an example needle trajectory in a porcine tissue phantom, as used in the ex vivo study. Needle entry and tip point were manually annotated in the 3D image to determine the ground truth needle path. (b) From the annotation, a 3D ground truth label image was created for the training of the CNN by connecting the tip and entry point with a gaussian-blurred line (standard deviation = 6 mm). (c) The needle orientation is characterized by the inclination angle θ of the needle path with the direction of B₀ (z-axis) and the azimuthal angle φ between the needle and the zy (sagittal)-plane.

Insertion depth was manually adjusted between 4 and 5 cm.

Ex vivo test dataset

To assess localization accuracy, the same 22-gauge needle as used for the training dataset was inserted into four additional ex vivo porcine tissue phantom, and a test dataset of WM and corresponding reference GRE images for ground truth needle path extraction (imag-

ing parameters as above) was acquired for a total of 109 needle trajectories (see description of ex vivo test dataset in Table 1). Needle orientations were sampled from a range of $\theta \in [78^\circ, 90^\circ]$ and $\varphi \in [0^\circ, 30^\circ]$ (therefore sampled only from within the parametric range of the training set) with manually adjusted insertion depths between 4 and 5 cm. Data was acquired using a spine coil (Siemens Healthineers AG, Erlangen, Germany) and a dedicated interventional loop coil (iLoop Interventional

2473429, 2024, 11, Downloaded from https://apm.onlinelibary.wiely.com/oi/10.1002/mp.17376 by Ddz Zentrabibishotek Krebsforschungszentrum, Wiley Online Library on [01/10/2025]. See the Terms and Conditions (https://onlinelibrary.wiely.com/terms-and-conditions) on Wiley Online Library for rules of use; OA articles are governed by the applicable Creative Commons License

Coil 0.55T; NORAS MRI products GmbH, Höchberg, Germany) as shown in the example in Figure 3a.

In vivo proof-of-concept experiment

In a proof-of-concept in vivo experiment, a 20-gauge and a 22-gauge MR-compatible aspiration needle (Cook Medical, Bloomington, Indiana, USA) were inserted into the thigh muscle of two pigs (see description of in vivo dataset in Table 1) and a WM image and corresponding reference GRE image for animal 1 and reference bSSFP images for animal 2 for the extraction of the ground truth needle path were acquired [GRE imaging parameters as above, bSSFP imaging parameters: FOV = (256 mm)³; image matrix = (128 px)³; TR = 5.56 ms; TE = 2.78 ms; flip angle = 70°; bandwidth = 558 Hz/pixel].

To evaluate the performance of the investigated localization method, the CNN was trained on the training dataset described above. To study feasible acceleration of the localization method, WM images were reconstructed from the acquired data using different numbers of retrospectively cropped k-space spokes: N₁ = 6434 (fully sampled for uniform radial k-space coverage²³), $N_2 = 256$, $N_3 = 128$, $N_4 = 64$, $N_5 = 32$, $N_6 = 16$. Depending on TR (TR₁ = 0.0125 s and TR₂ = 0.015s used for ex vivo and in vivo dataset, respectively, as shown in Table 1), this corresponds to acquisition times $t_{acq}(N_1, TR_1) = 80.4 \text{ s}, t_{acq}(N_2, TR_1) = 3.2 \text{ s}, t_{acq}(N_3, TR_1)$ TR_1) = 1.6 s, $t_{acq}(N_4, TR_1) = 0.8$ s, $t_{acq}(N_5, TR_1) = 0.4$ s, $t_{acq}(N_6, TR_1) = 0.2 \text{ s}$ and $t_{acq}(N_1, TR_2) = 96.5 \text{ s}$, $t_{acq}(N_2, TR_2) = 3.8 \text{ s}, t_{acq}(N_3, TR_2) = 1.9 \text{ s}, t_{acq}(N_4, TR_2)$ TR_2) = 1.0 s, $t_{acq}(N_5, TR_2) = 0.5$ s, $t_{acq}(N_6, TR_2) = 0.2$ s. For each undersampling factor, a separate CNN model was trained to regress from the (undersampled) WM image to the needle path (label image) using an L2 loss function and a Stochastic Gradient Decent (SGD) optimizer (number of epochs = 200; learning rate = 0.1; decay = 1e-6; momentum = 0.9; batch size = 8), resulting in a total of six trained models for the corresponding sampling numbers N_1 to N_6 .

2.2.3 Accuracy metrics and performance evaluation

To evaluate the localization accuracy, two metrics were defined (Figure 5). $\Delta\alpha$ describes the angle between the ground truth needle axis and the detected needle axis. Hence, it describes the maximum angular deviation of an automatically selected imaging plane and the needle axis. If $\Delta\alpha$ is zero, the needle is parallel to the selected plane. $\Delta\alpha$ is a commonly used metric for the evaluation of detected needle orientation.^{7,14} Δ s was defined as the distance between the ground truth needle tip position

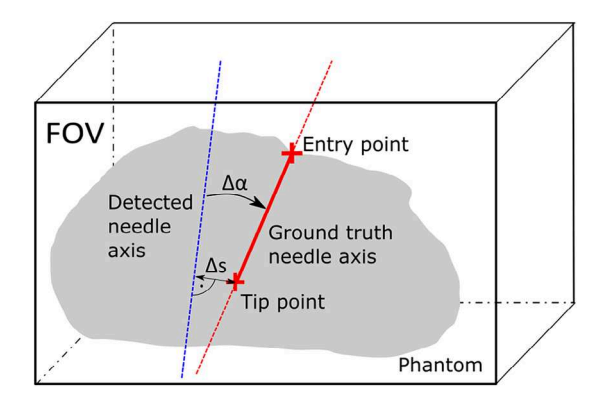


FIGURE 5 Two metrics were defined for performance evaluation of the implemented localization algorithm: Δs is the distance between the ground truth needle tip and the detected needle axis and $\Delta \alpha$ is the angular deviation between the ground truth needle axis and the detected needle axis.

and the detected needle axis. Therefore, Δs describes the maximum distance of the tip to an automatically selected imaging plane. If Δs is too large, the tip will not be visible in the 2D image. Mehrtash et al. had proposed a similar metric, measuring the distance of the needle tip to a selected axial plane. Our proposed metric Δs is a slightly more general measure as it does not restrict the chosen plane to an axial plane but holds as an upper limit for the distance "needle tip to selected plane" for arbitrary plane orientations. $\Delta \alpha$ and Δ s were analyzed for the samples from the acquired ex vivo test dataset and the in vivo experiment. To investigate the influence of the needle's inclination angle relative to B₀ on the achieved localization accuracy, the samples from the test dataset were binned into three subsets covering three ranges of inclination angles: $\theta \in (86^{\circ}, 90^{\circ}]; \theta \in (82^{\circ}, 86^{\circ}]; \theta \in$ (78°,82°]. The median (± median absolute deviation) of Δ s and $\Delta\alpha$ was calculated for all subsets.

The required needle localization accuracy for a successful imaging plane alignment generally depends on the chosen 2D imaging slice thickness, the needle size, and the size of the needle artifact. Tip visibility is especially crucial during interventions, e.g., to confirm correct targeting of a suspicious lesion. The impact of the defined metric Δs is, therefore, in particular of clinical interest to the interventionalist. Consequently, a needle localization for a successful automatic slice positioning requires a small Δs . We investigated the rate of successful localizations in the ex vivo study by determining a threshold and requiring Δs to be smaller than this threshold. The success rate of the localization (number of samples with Δs < threshold / number of total samples) was determined for the three angular bins described above and for three different thresholds $(\Delta s < 4 \text{ mm}; \Delta s < 8 \text{ mm}; \Delta s < 12 \text{ mm})$. Feasibility of automatic slice alignment was additionally demonstrated by retrospectively reformatting a 2D imaging slice from a 3D reference image based on the detected needle position and orientation for the in vivo experiments and two example needle insertions from the ex vivo test dataset.

3 RESULTS

Loss curves for training of the U-Net models with sampling numbers N₁ to N₆ are given in supplementary Figure S1. An overview on training, validation, and test loss values is given in Supplementary Table S1.

On standard PC hardware (Core i7-10850H CPU with 2.70 GHz base frequency; Intel, Santa Clara, California, USA; Quadro T2000 GPU; Nvidia, Santa Clara, California, USA), retrospective localization took between 2 and 41 s per acquisition (reconstruction times for three reconstructed coil channels on CPU (non-parallelized): $t_{\text{recon}} = 39.4 \text{ s for } 6434 \text{ spokes}, t_{\text{recon}} = 1.9 \text{ s for } 256$ spokes, $t_{recon} = 1.2 \text{ s}$ for 128 spokes, $t_{recon} = 0.8 \text{ s}$ for 64 spokes, $t_{recon} = 0.6$ s for 32 spokes, $t_{recon} = 0.5$ s for 16 spokes; processing time of needle localization algorithm < 1 s).

3.1 Needle localization

Figure 6 shows two representative localizations (for 6434, 256, 64, and 32 sampled k-space spokes) from the evaluated ex vivo test dataset. In the example shown in Figure 6a, the needle is oriented with an inclination of $\theta = 88.1^{\circ}$, therefore approximately perpendicular to the B₀ field. Despite increased noise, the WM needle artifact remains clearly visible for images reconstructed from fewer k-space spokes and a localization accuracy of $\Delta \alpha \leq 3.4^{\circ}$ and $\Delta s \leq 2.5$ mm could be achieved for as few as 32 k-space spokes. For the example shown in Figure 6b, the needle enclosed an angle of $\theta = 78.2^{\circ}$ with B_0 . Visibility of the WM needle artifact decreased for fewer sampled k-space spokes. For 32 spokes, the needle artifact can almost no longer be delineated from the noisy background in the WM image. While a needle localization accuracy of $\Delta \alpha \leq 3.8^{\circ}$ and $\Delta s \leq$ 2.2 mm could be achieved for images reconstructed from 6434, 256, and 64 spokes, accuracy decreased for the image reconstructed from 32 spokes to $\Delta \alpha = 13.9^{\circ}$ and $\Delta s = 8.3$ mm.

In Table 2, the medians of the metrics $\widetilde{\Delta \alpha}$ and Δs (\pm the median absolute deviation) are displayed for all investigated undersampling factors with the samples of the test dataset binned for the needle inclination angle θ . For 6434, 256, 64, and 32 spokes, the achieved accuracies for the metrics are additionally visualized as boxplots (Figure 7) for the inclination-binned test dataset samples. Median accuracy across the binned samples from the test set can be seen to decrease with a lower number of spokes, as well as needle trajectories increasingly parallel to the B₀ field. For inclination

The test set was binned into three subsets with n samples, characterized by different needle inclination angles θ. For each subset, the median (± the median absolute deviation) of 2 TABLE

the achieved accu	the achieved accuracy was calculated for the introduced metrics	troduced metrics $\Delta lpha$ and Δs . R	results are color-coded for Δ	$\Delta \alpha$ and Δs . Results are color-coded for Δs : White \triangleq (4 mm > Δs); light grey \triangleq (8 mm > $\Delta s \ge 4$ mm); dark grey \triangleq ($\Delta s \ge 8$ mm).	grey \triangleq (8 mm > Δ s \geq 4 mm);	dark grey $\triangleq (\Delta s \ge 8 \text{ mm})$.
	6434 spokes (fully sampled)	256 spokes	128 spokes	64 spokes	32 spokes	16 spokes
$n = 36$ $\theta \in (86^{\circ}, 90^{\circ}]$	$\widetilde{\Delta\alpha} = (2.6 \pm 1.4)^{\circ}$ $\widetilde{\Delta s} = (1.9 \pm 0.6) \text{ mm}$	$\widetilde{\Delta\alpha} = (2.1 \pm 0.8)^{\circ}$ $\widetilde{\Delta s} = (1.6 \pm 0.5) \text{ mm}$	$\widetilde{\Delta \alpha} = (2.8 \pm 0.7)^{\circ}$ $\widetilde{\Delta S} = (1.9 \pm 0.5) \text{ mm}$	$\widetilde{\Delta \alpha} = (4.1 \pm 1.4)^{\circ}$ $\widetilde{\Delta s} = (2.6 \pm 0.7) \text{ mm}$	$\frac{\widetilde{\Delta\alpha}}{\widetilde{\Delta S}} = (4.7 \pm 2.1)^{\circ}$ $\frac{\widetilde{\Delta S}}{\widetilde{\Delta S}} = (3.1 \pm 1.2) \text{ mm}$	$\widetilde{\Delta \alpha} = (9.5 \pm 4.7)^{\circ}$ $\widetilde{\Delta S} = (4.7 \pm 3.0) \text{ mm}$
n = 40 $\theta \in (82^{\circ}, 86^{\circ}]$	$\widetilde{\Delta\alpha} = (2.3 \pm 0.9)^{\circ}$ $\widetilde{\Delta s} = (1.5 \pm 0.5) \text{ mm}$	$\widetilde{\Delta \alpha} = (2.2 \pm 0.8) \text{ mm}$ $\widetilde{\Delta s} = (1.7 \pm 0.7)^{\circ}$	$\widetilde{\Delta \alpha} = (3.0 \pm 1.4)^{\circ}$ $\widetilde{\Delta S} = (1.8 \pm 0.8) \text{ mm}$	$\widetilde{\Delta \alpha} = (3.7 \pm 1.6)^{\circ}$ $\widetilde{\Delta s} = (2.6 \pm 1.1) \text{ mm}$	$\widetilde{\Delta \alpha} = (7.7 \pm 2.6)^{\circ}$ $\widetilde{\Delta s} = (4.6 \pm 2.5) \text{ mm}$	$\widetilde{\Delta\alpha} = (15.6 \pm 9.3)^{\circ}$ $\widetilde{\Delta s} = (13.7 \pm 12.7) \text{ mm}$
$n = 33$ $\theta \in (78^{\circ}, 82^{\circ}]$	$\widetilde{\Delta\alpha} = (2.5 \pm 1.1)^{\circ}$ $\widetilde{\Delta s} = (2.2 \pm 0.7) \text{ mm}$	$\widetilde{\Delta\alpha} = (2.5 \pm 1.1)^{\circ}$ $\widetilde{\Delta s} = (1.9 \pm 0.5) \text{ mm}$	$\widetilde{\Delta\alpha} = (5.2 \pm 3.0)^{\circ}$ $\widetilde{\Delta s} = (2.6 \pm 1.1) \text{ mm}$	$\widetilde{\Delta\alpha} = (6.8 \pm 2.7)^{\circ}$ $\widetilde{\Delta s} = (3.5 \pm 1.5) \text{ mm}$	$\widetilde{\Delta \alpha} = (13.5 \pm 7.7)^{\circ}$ $\widetilde{\Delta S} = (9.1 \pm 7.2) \text{ mm}$	$\widetilde{\Delta\alpha} = (30.8 \pm 9.0)^{\circ}$ $\widetilde{\Delta s} = (53.0 \pm 17.9) \text{ mm}$

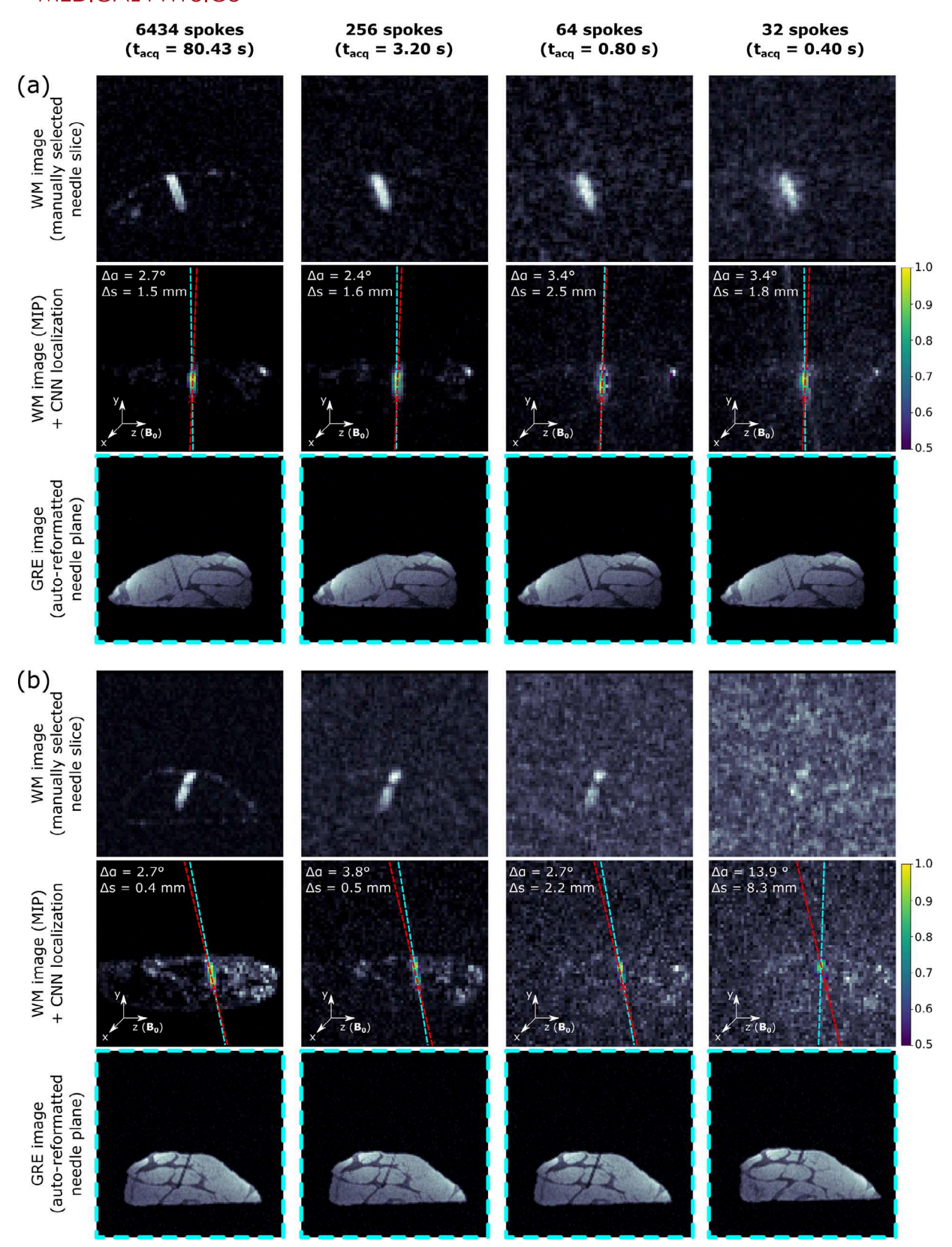


FIGURE 6 Two examples from the test dataset with inclination angles $\theta = 88.1^{\circ}$ (a) and $\theta = 78.2^{\circ}$ (b) to the B₀ field. The first row shows a manually selected slice of the acquired (undersampled) 3D WM image which contains the WM needle artifact. The second row shows the 3D WM image as maximum intensity projection (MIP) with an overlay of the CNN localization. The red cross marks the ground truth needle tip and the red dashed line the ground truth needle axis, the blue dashed line marks the predicted needle axis. The third row shows a reformatted 2D slice from the reference 3D spoiled GRE image (slice thickness = 4 mm), where the slice position and orientation (tilted transversal slice) were automatically chosen based on the detected needle path.

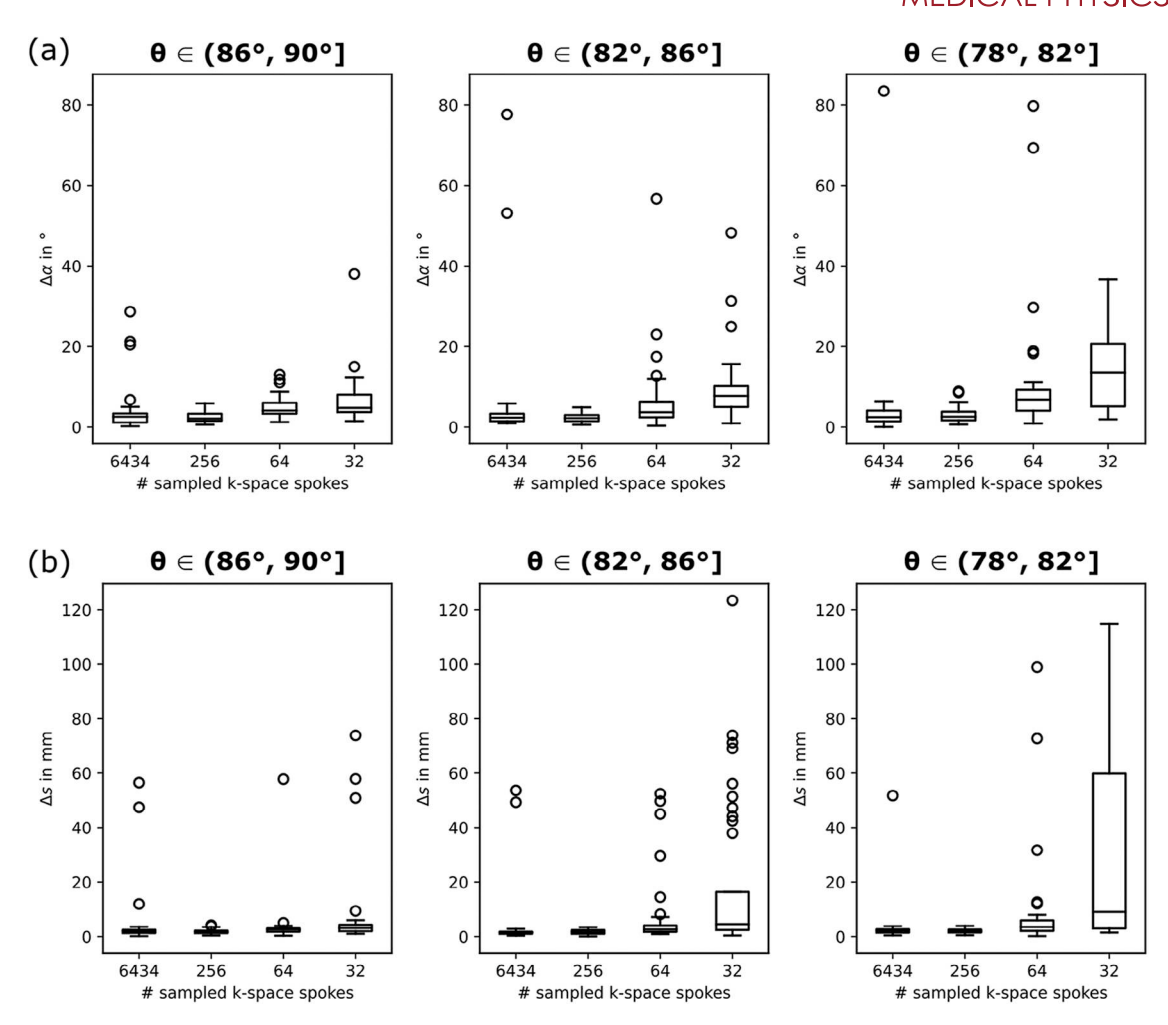


FIGURE 7 Performance analysis of the investigated needle localization technique. The ex vivo test dataset was split into three subsets with varying inclination angle θ . The angular deviation $\Delta\alpha$ (a) and the tip distance Δ s (b) are displayed as boxplots for various undersampling factors (6434, 256, 64, and 32 sampled k-space spokes). Boxes extend over interquartile range (IQR) with whiskers covering 1.5 x IQR. Outliers are displayed as circles. Medians are indicated by black crosslines.

angles $\theta=(86^\circ,90^\circ]$, we find $\widetilde{\Delta\alpha}=(2.6\pm1.4)^\circ$ and $\widetilde{\Delta s}=(1.9\pm0.6)$ mm, as well as $\widetilde{\Delta\alpha}=(9.5\pm4.7)^\circ$ and $\widetilde{\Delta s}=(4.7\pm3.0)$ mm, for 6434 and 16 spokes, respectively. For, e.g., 64 spokes, achieved median accuracy decreases from $\widetilde{\Delta\alpha}=(4.1\pm1.4)^\circ$ and $\widetilde{\Delta s}=(2.6\pm0.7)$ for $\theta=(86^\circ,90^\circ]$ to $\widetilde{\Delta\alpha}=(6.8\pm2.7)^\circ$ and $\widetilde{\Delta s}=(3.5\pm1.5)$ mm for $\theta=(78^\circ,82^\circ)$].

Figure 8 shows the needle localization for the in vivo proof-of-concept experiments for $N_1=6434$ to $N_5=32$ acquired k-space spokes. For needle insertions close to the transversal plane, localization results of $\Delta\alpha=3.4^\circ$ and $\Delta s=1.4$ mm (Figure 8a), as well as $\Delta\alpha=4.1^\circ$ and $\Delta s=6.9$ mm (Figure 8b) for as few as 32 sampled k-space spokes were achieved. For Figure 8c (needle tilted out of the transversal plane), localization with $\Delta\alpha=6.8^\circ$ and $\Delta s=5.3$ mm could be achieved for as few as 128 sampled k-space spokes. Localization failed for 64 and 32 sampled spokes.

3.2 | Automatic slice alignment

For both ex vivo examples in Figure 6, a 2D slice oriented along the detected needle axis was reformatted from the respective 3D GRE reference image to retrospectively investigate feasibility of automatic slice alignment. In the example in Figure 6a, the needle is fully visible in the automatically selected slice for all investigated undersampling factors. While the needle artifact was fully visible for 6434 to 64 k-space spokes in the example of Figure 6b, the detected needle axis was too oblique to the true needle path for needle localization below 64 spokes, so that the needle moved out of the reformatted plane and the tip is no longer visible.

In Table 3, the achieved localization success rate for the ex vivo study (defined as Δs being below a certain threshold) is displayed. The success rate decreases with higher undersampling and greater inclination of the needle to the B_0 field. A success rate of \geq 72% could be

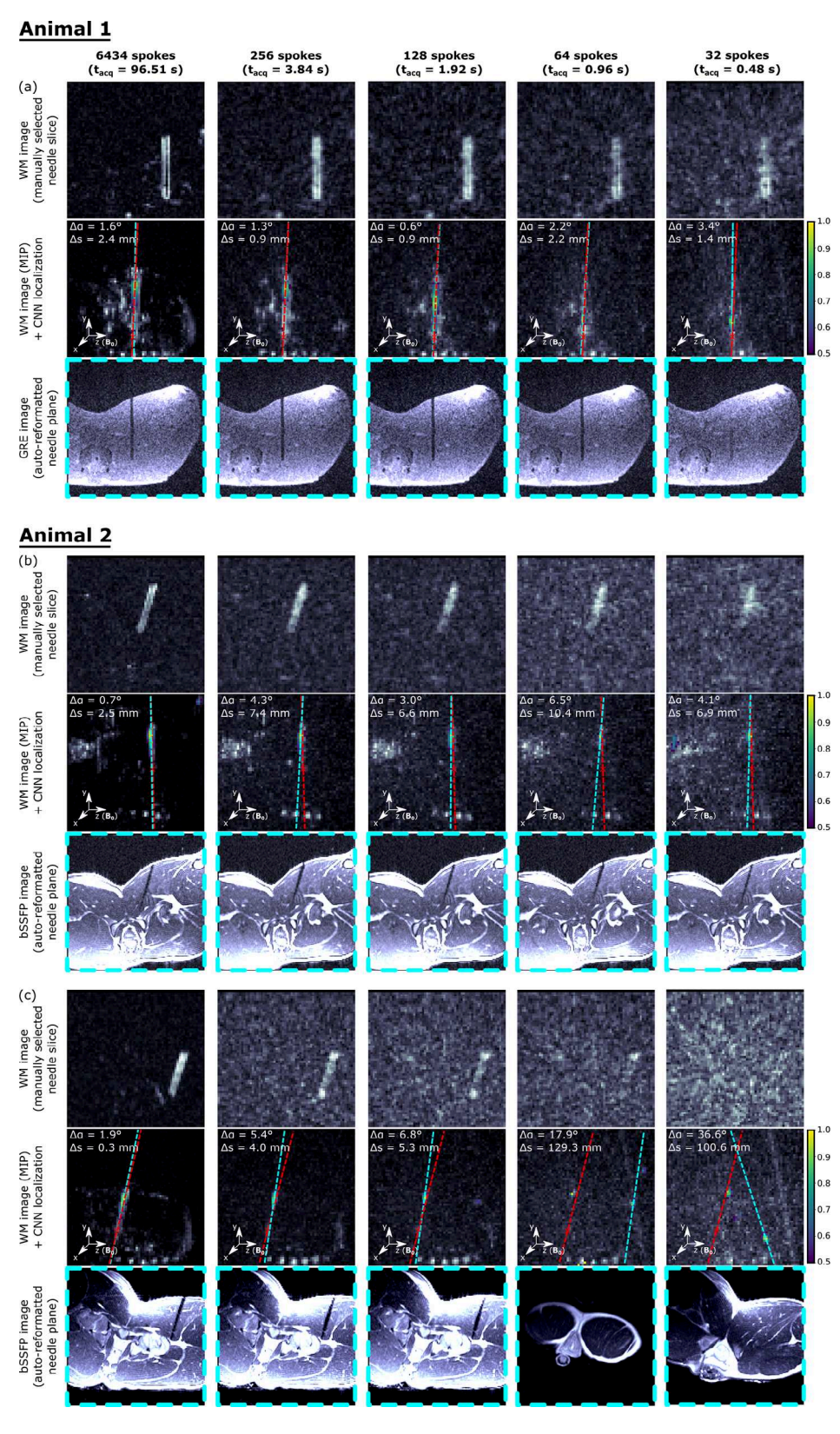


FIGURE 8 Proof-of-principle in vivo experiments with two porcine animal models. A 20-gauge (a) and a 22-gauge (b,c) aspiration needle were inserted into the thigh of two pigs and images were acquired with a spine and a loop coil (a,c) and a spine and a flex coil (b), respectively. The needles were inserted with an inclination angle to B_0 of (a) $\theta_1 = 87.7^\circ$, (b) $\theta_2 = 88.8^\circ$, and (c) $\theta_3 = 77.6^\circ$. Similar to Figure 5, the first row of each subfigure shows a manually selected slice from the (undersampled) 3D WM image. The needle WM artifact, as well as residual WM artifacts from the tissue, is visible. The second row shows the CNN prediction as overlay to a MIP of the WM image. The third row shows a reformatted slice (slice thickness = 4 mm) from a 3D GRE/bSSFP reference dataset that was selected based on the automatic localization of the needle.

TABLE 3 The test set was binned into three subsets with varying inclination angle θ . The proportion of samples was calculated for which a distance $\Delta s < 4$ mm, $\Delta s < 8$ mm or $\Delta s < 12$ mm was achieved (success rate). Results are color-coded for the success rate: White \triangle (success rate \ge 75%); light grey \triangle (75% > success rate \ge 50%); dark grey \triangle (success rate < 50%).

	Θ ∈ (86°,90°]					
	Fully sampled	256 spokes	128 spokes	64 spokes	32 spokes	16 spokes
No. of samples with $(\Delta s < 4 \text{ mm})$ / total no. of samples	33/36 = 92%	35/36 = 97%	36/36 = 100%	34/36 = 94%	26/36 = 72%	17/36 = 47%
No. of samples with $(\Delta s < 8 \text{ mm})$ / total no. of samples	33/36 = 92%	36/36 = 100%	36/36 = 100%	35/36 = 97%	32/36 = 89%	24/36 = 67%
No. of samples with $(\Delta s < 12 \text{ mm})$ / total no. of samples	34/36 = 94%	36/36 = 100%	36/36 = 100%	35/36 = 97%	33/36 = 92%	28/36 = 78%
	<i>θ</i> ∈ (82°,86°]					
	Fully sampled	256 spokes	128 spokes	64 spokes	32 spokes	16 spokes
No. of samples with $(\Delta s < 4 \text{ mm})$ / total no. of samples	38/40 = 95%	40/40 = 100%	35/40 = 88%	29/40 = 72%	18/40 = 45%	12/40 = 30%
No. of samples with $(\Delta s < 8 \text{ mm})$ / total no. of samples	38/40 = 95%	40/40 = 100%	38/40 = 95%	34/40 = 85%	29/40 = 72%	16/40 = 40%
No. of samples with $(\Delta s < 12 \text{ mm})$ / total no. of samples	38/40 = 95%	40/40 = 100%	38/40 = 95%	35/40 = 88%	30/40 = 75%	19/40 = 48%
	<i>θ</i> ∈ (78°,82°]					
	Fully sampled	256 spokes	128 spokes	64 spokes	32 spokes	16 spokes
No. of samples with $(\Delta s < 4 \text{ mm})$ / total no. of samples	32/33 = 97%	33/33 = 100%	21/33 = 64%	19/33 = 58%	11/33 = 33%	3/33 = 9%
No. of samples with $(\Delta s < 8 \text{ mm})$ / total no. of samples	32/33 = 97%	33/33 = 100%	27/33 = 82%	28/33 = 85%	15/33 = 45%	4/33 = 12%
No. of samples with $(\Delta s < 12 \text{ mm})$ / total no. of samples	32/33 = 97%	33/33 = 100%	28/33 = 85%	28/33 = 85%	18/33 = 55%	6/33 = 18%

achieved for a threshold of $\Delta s = 4$ mm across all investigated undersampling factors between 6434 and 32 spokes for inclination angles $\theta = (86^{\circ}, 90^{\circ}]$. For $\theta = (78^{\circ}, 82^{\circ}]$, a success rate of $\geq 82\%$ could still be achieved for a threshold of $\Delta s = 8$ mm for as few as 64 spokes.

For the investigated in vivo cases, the needle path was fully visible in the reformatted 2D GRE slice in the example of Figure 8a for images reconstructed from 6434 to 64 k-space spokes ($\Delta \alpha < 2.2^{\circ}$; $\Delta s < 2.4$ mm). The detected needle axis was slightly more oblique to the true needle axis and the needle artifact moves out of the automatically reformatted image plane for the needle localization on the 32-spoke image ($\Delta \alpha = 3.4^{\circ}$; $\Delta s = 1.4$ mm). However, the tip of the needle is still visible in the automatically aligned plane. For the example in Figure 8b, the needle is visible in all reformatted 2D bSSFP slices. Tip visibility is limited except for the fully-sampled case with ∆s exceeding the chosen slice thickness of 4 mm. For case Figure 8c, automatic plane alignment was successful for images reconstructed from 6434 ($\Delta \alpha = 1.9^{\circ}$; $\Delta s = 0.3$ mm) to 128 spokes ($\Delta \alpha = 6.8^{\circ}$; $\Delta s = 5.3$ mm). As needle localization failed for higher acceleration factors (64 and 32 spokes), slice alignment was not feasible.

4 | DISCUSSION

In this work, a method for rapid 3D needle localization from WM images via a CNN-based algorithm for the purpose of automatic imaging slice alignment was implemented and evaluated. The proposed technique was successfully demonstrated in an ex vivo study and an in vivo proof-of-concept experiment by localizing needles from retrospectively undersampled images. Feasibility of automatic slice repositioning was demonstrated retrospectively.

High undersampling factors allowed for rapid localization of needles oriented approximately perpendicular to B₀. In the conducted ex vivo study, localization accuracy was found to generally decrease with fewer sampled kspace spokes and for needle trajectories increasingly parallel with B_0 . For the conducted in vivo experiments, needle localization for a needle insertion tilted out of the transversal plane was equally found to be more challenging than for needle placements approximately orthogonal to the orientation of the B₀ field. While the WM needle artifact is clearly visible in the fully reconstructed images in the examples of Figure 6 from the ex vivo dataset, image noise can be seen to impair the visibility of the needle artifact for images reconstructed from an increasingly undersampled k-space. As the signal magnitude of the WM needle artifact is reduced for smaller inclination angles as demonstrated in Figure 2c, it was increasingly difficult to delineate the WM needle artifact against the background for low numbers of sampled k-space spokes. The reduced visibility of the

needle artifact appeared to confound the correct determination of the needle's position and orientation by the CNN, leading to reduced localization accuracy for fewer sampled k-space spokes and inclination angles closer to B₀. In the conducted ex vivo study, inclination angles sampled from a range $\theta = [78^\circ, 90^\circ]$ were investigated. Accuracy is expected to further decrease for angles outside this range, essentially limiting the proposed rapid localization technique to needle trajectories close to the transversal plane. Transversal trajectories are, however, common for many MR-guided needle interventions.²⁴

Rapid 3D needle localization as investigated in this work can enable automatic slice repositioning in MRguided interventions. Based on the determined device position and orientation, 2D real-time imaging planes will be aligned with the needle, ensuring needle visibility. Without a method for automatic slice positioning, manual iterative repositioning of the imaging planes by the MR technician is necessary. Manual repositioning requires additional time with full attention to the repositioning procedure. For the automatic positioning of a 2D imaging slice, the required accuracy of the needle localization will depend on the utilized slice thickness, but also on the needle size and the size of the needle artifact. Image plane alignment using the proposed rapid 3D needle localization method was successfully demonstrated retrospectively for ex vivo and in vivo needle insertions. Although tip visibility was limited in the in vivo example of Figure 8b for an accelerated image acquisition (slice thickness of 4 mm too aggressive for achieved Δs), the reached partial slice alignment will still be of high value during an intervention if the needle was lost from the 2D real-time images before. A partial slice alignment can serve as a starting point for manual readjustment, or, alternatively, a method acquiring several adjacent slices to automatically correct for slight misalignments of the needle as proposed by Li et al. 14 could be used. Slice thickness can also be increased to better visualize the needle tip. It was shown that, taking the tip-to-predicted needle axis distance (Δ s) as an indicator of a successful slice positioning, satisfactory results can generally be achieved with the proposed technique from fully sampled images, as well as for an accelerated image acquisition (Table 3). Sampling only 16 k-space spokes still yielded successful results in some cases for needle orientations approximately orthogonal to B₀. It is important to note that such a large reduction of sampled k-space (402-fold acceleration compared to full radial k-space sampling) is most likely not required for the use case of automatic slice positioning. Even for lower undersampling and, therefore, higher acquisition times, the method can still be rapid enough to enhance the workflow of an intervention, as a manual adjustment of a slice position can involve multiple iterative steps and would typically require more time. Therefore, our method has the potential to speed up the MR interventional workflow.

While the image processing time of the localization algorithm was constant, reconstruction times for the 3D WM images varied with the implemented off-line reconstruction, depending on the number of sampled spokes. Image reconstruction times can be further decreased by using dedicated hardware, e.g., GPUs.²⁵ For an application of the investigated localization method for automatic slice repositioning during an intervention, a new slice alignment would, in many cases, also not be required to be interleaved with every single 2D real-time measurement. It could, e.g., be triggered by the user with a button click on an on-demand basis. In practice, a user of the investigated method could balance a required threshold of Δs with the acceptable acquisition time for the localization, as the implemented Golden Angle sampling for the radial WM-encoded sequence allows to dynamically adapt the number of acquired radial k-space lines. As described above, the ideal number of acquired k-space spokes to balance time efficiency and localization accuracy, i.e., to reach a certain threshold of Δs , depends on needle angulation and required slice thickness of realtime imaging planes, whereby the choice of a certain slice thickness can depend, e.g., on the size of the targeted lesion, the type and size of the needle and the size of the needle artifact.

The CNN used for the localization was trained on ex vivo porcine tissue phantoms, which were placed in a head coil to simplify the data acquisition of the training set (the set-up allowed to easily move, switch, and rotate phantoms for the fast generation of training data). As demonstrated by the successful localization, the network generalized well to the dedicated interventional coil set-up (loop + spine coil) used for the ex vivo test dataset, as well as the in vivo animal experiment (loop + spine coil and flex + spine coil), where a slightly different needle type was used for animal 1. The in vivo set-up also involved more complex anatomy, and therefore different background artifacts, a different needle insertion depth as well as slightly different imaging parameters (changed bandwidth and TR). This indicates a high robustness of the CNN-based WM needle detection. Future work will further explore the reliability of the proposed method, especially when translating the technique to more challenging in vivo scenarios where patient motion can be expected (e.g., breathing for interventions in the abdomen). However, as described above, the Golden Angle approach allows to adapt the number of acquired k-space spokes, and therefore the acquisition time, to the expected amount of patient motion.

Various approaches for MR needle localization for the purpose of automatic slice alignment have been investigated in the past. As described in the Introduction, Reichert et al. 11 localized a marker attached to a needle outside the body using two undersampled 2D tracking slices. An accuracy of 1 mm was reported, acquiring in total four radial lines of k-space. The use of an external

marker and the requirement to pre-position the tracking slice might pose constraints for certain workflows compared to a direct localization approach of the needle with the 3D WM concept proposed in this work. As the marker is localized and not directly the needle, possible bending of the needle inside the body tissue also must be taken into consideration. Using three echo-dephased spatial projections, Patil et al. could localize a paramagnetic marker, which can be attached to interventional devices, with an accuracy of 4.5 mm.¹² As no information on the orientation of the device is extracted, the technique would, compared to the proposed method of this work, not allow for the alignment of a slice with a needle trajectory. Using a 3D CNN-based localization approach, Mehrtash et al⁷ achieved an average accuracy of 2.80 mm for needle tip localization and 0.98° deviation for needle orientation. With acquisition times on the order of one minute for the acquired conventional spin-echo images, the technique is not optimized for the application of automatic slice alignment in realtime workflows in contrast to the proposed method of this work, which was specifically designed for rapid 3D needle localization. Also using a CNN-based approach, Li et al. localized the needle in a slab (thickness of 15 mm) of three 2D slices with a median accuracy of 2.2 mm in position and 1.2° in orientation. 14 Compared to the proposed fully 3D-based method of this work, the technique requires prior information on the needle position and orientation to align the imaging slices. While both these CNN-based needle localization methods use loss functions related to cross-entropy and dice loss as commonly used in segmentation tasks, we have decided to implement L2 (mean squared error) loss to train our network. Needle artifact appearance depends on needle type and material parameters, as well as sequence type (spin-echo vs. gradient echo) and sequence parameters.⁴ It is, therefore, not straightforward to determine the position of the needle axis from the needle artifact. It has been shown, however, that CNNs can regress from the needle artifact to the needle axis.14 The aim of retrieving the needle axis/needle vector from the input White-Marker images can, therefore, be seen as a regression task, rather than a pure segmentation task, with the squared L2 norm being a common loss function for regression tasks.²⁶ Creating an accurate binary segmentation label of the White-Marker needle artifact and the background would also require a manual pixelwise annotation in 3D. The creation of a Gaussian heatmap of the needle axis as used in the regression task requires only the marking of two positions and is a lot more time efficient. Recently, Zhou et al.27 proposed the use of a vision transformer as an alternative to the CNN architecture for Deep-Learning based needle segmentation from 3D intra-procedural MR images, delivering promising results (1.48 mm and 0.98° for tip- and axis localization error). While their implementation was not intended to

2473429, 2024, 11, Downloaded from https://apm.onlinelibary.wiely.com/oi/10.1002/mp.17376 by Ddz Zentrabibishotek Krebsforschungszentrum, Wiley Online Library on [01/10/2025]. See the Terms and Conditions (https://onlinelibrary.wiely.com/terms-and-conditions) on Wiley Online Library for rules of use; OA articles are governed by the applicable Creative Commons License

be used for real-time slice alignment (acquisition time 13 s), the implementation of a transformer architecture into our 3D WM framework could pose a future development step and might enable direct image-to-needle vector regression without the requirement of a PCA postprocessing step, which is challenging with the CNN architecture.²⁸ However, more training data might be required to achieve good localization accuracy.²⁹

The rapid 3D localization technique investigated in this work can be seen as complementary to 2D tracking approaches. Existing 2D needle localization techniques reach submillimeter accuracy for tip localization and allow the determination of the needle orientation in the 2D slice with an accuracy on the order of one degree.^{6,9,13} For all 2D techniques, position and orientation of a slice containing the needle must be known beforehand. In contrast, the 3D approach investigated in this work enables localization of the needle without prior knowledge of the location and automatic positioning of a 2D imaging slice, and in this way could be included in real-time imaging sequences as a fast tracking block. A 2D tracking technique can then subsequently be used to follow motion of the needle in the 2D imaging slice for accurate needle tip localization. The 3D WM approach could also be used to reduce the manual steps that are required to reposition the 2D imaging plane when the needle is not visible in the chosen slice, e.g., because the planned and actual needle trajectory or needle insertion point do not match, or the needle is lost from the slice due to patient motion.

5 | CONCLUSION

In this work, we proposed, implemented, and evaluated a novel method for rapid CNN-based 3D passive needle localization using a WM acquisition for application in automatic slice positioning to facilitate MR-guided needle interventions. The method was investigated in an ex vivo study. Needle localization was also successfully demonstrated in in vivo proof-of-concept experiments. The investigated approach was shown to allow for fast localization of a needle without prior knowledge of its location. This can potentially enable speed up of percutaneous needle intervention workflows, since it can help to avoid manual positioning steps for the 2D real-time imaging planes.

ACKNOWLEDGMENTS

The authors have nothing to report.

CONFLICT OF INTEREST STATEMENT

Jonas F. Faust, Axel J. Krafft, Daniel Polak, Peter Speier, Nicolas G. R. Behl, and Florian Maier are employees of Siemens Healthineers AG. Nathan Ooms, Jesse Roll and Joshua Krieger are employees of Cook Advanced Technologies. Mark E. Ladd has no relevant conflict of interest to disclose.

REFERENCES

- Veltri A, Bargellini I, Giorgi L, Almeida PAMS, Akhan O. CIRSE Guidelines on Percutaneous Needle Biopsy (PNB). Cardiovasc Intervent Radiol. 2017;40(10):1501-1513.
- Weiss CR, Nour SG, Lewin JS. MR-guided biopsy: a review of current techniques and applications. J Magn Reson Imaging. 2008;27(2):311-325.
- Rothgang E, Gilson WD, Wacker F, Hornegger J, Lorenz CH, Weiss CR. Rapid freehand MR-guided percutaneous needle interventions: an image-based approach to improve workflow and feasibility. J Magn Reson Imaging. 2013;37(5):1202-1212.
- Lewin JS, Duerk JL, Jain VR, Petersilge CA, Chao CP, Haaga JR. Needle localization in MR-guided biopsy and aspiration: effects of field strength, sequence design, and magnetic field orientation. Am J Roentgenol. 1996;166(6):1337-1345.
- Seppenwoolde JH, Viergever MA, Bakker CJG. Passive tracking exploiting local signal conservation: the white marker phenomenon. Magn Reson Med. 2003;50(4):784-790.
- Li X, Young AS, Raman SS, et al. Automatic needle tracking using Mask R-CNN for MRI-guided percutaneous interventions. Int J Comput Assist Radiol Surg. 2020;15(10):1673-1684.
- Mehrtash A, Ghafoorian M, Pernelle G, et al. Automatic needle segmentation and localization in MRI with 3-D convolutional neural networks: application to MRI-targeted prostate biopsy. *IEEE Trans Med Imaging*. 2019;38(4):1026-1036.
- Ronneberger O, Fischer P, Brox T. U-Net: convolutional networks for biomedical image segmentation. In: Navab N, Hornegger J, Wells WM, Frangi AF, eds. Medical Image Computing and Computer-Assisted Intervention—MICCAI 2015. Springer International Publishing; 2015:234-241.
- Weine J, Breton E, Garnon J, Gangi A, Maier F. Deep learning based needle localization on real-time MR images of patients acquired during MR-guided percutaneous interventions.
 Proceedings of the 27th Annual Meeting of ISMRM; 2019:0973.
- De Oliveira A, Rauschenberg J, Beyersdorff D, Semmler W, Bock M. Automatic passive tracking of an endorectal prostate biopsy device using phase-only cross-correlation. *Magn Reson Med*. 2008;59(5):1043-1050.
- Reichert A, Reiss S, Krafft AJ, Bock M. Passive needle guide tracking with radial acquisition and phase-only cross-correlation. *Magn Reson Med.* 2021;85(2):1039-1046.
- Patil S, Bieri O, Jhooti P, Scheffler K. Automatic slice positioning (ASP) for passive real-time tracking of interventional devices using projection-reconstruction imaging with echo-dephasing (PRIDE). Magn Reson Med. 2009;62(4):935-942.
- Zijlstra F, Viergever MA, Seevinck PR. SMART tracking: simultaneous anatomical imaging and real-time passive device tracking for MR-guided interventions. *Phys Med*. 2019;64:252-260.
- Li X, Lee YH, Lu DS, Tsao TC, Wu HH. Physics-driven Mask R-CNN for physical needle localization in MRI-guided percutaneous interventions. *IEEE Access*. 2021;9:161055-161068.
- Zur Y, Wood ML, Neuringer LJ. Spoiling of transverse magnetization in steady-state sequences. Magn Reson Med. 1991;21(2):251-263.
- Leupold J, Hennig J, Scheffler K. Moment and direction of the spoiler gradient for effective artifact suppression in RF-spoiled gradient echo imaging. Magn Reson Med. 2008;60(1):119-127.
- Chan RW, Ramsay EA, Cunningham CH, Plewes DB. Temporal stability of adaptive 3D radial MRI using multidimensional golden means. Magn Reson Med. 2009;61(2):354-363.
- Ladd ME, Erhart P, Debatin JF, Romanowski BJ, Boesiger P, McKinnon GC. Biopsy needle susceptibility artifacts. Magn Reson Med. 1996;36(4):646-651.

- Pipe JG, Menon P. Sampling density compensation in MRI: rationale and an iterative numerical solution. *Magn Reson Med*. 1999;41(1):179-186.
- Ong F, Lustig M. SigPy: a python package for high performance iterative reconstruction. *Proceedings of the 27th Annual Meeting* of *ISMRM*: 2019:4819.
- Çiçek Ö, Abdulkadir A, Lienkamp SS, Brox T, Ronneberger O.
 U-Net: learning dense volumetric segmentation from sparse annotation. In: Ourselin S, Joskowicz L, Sabuncu MR, Unal G, Wells W, eds. Medical Image Computing and Computer-Assisted Intervention—MICCAI 2016. Springer International Publishing; 2016:424-432.
- Zhao Y, Zeng K, Zhao Y, et al. Deep learning solution for medical image localization and orientation detection. *Med Image Anal*. 2022;81:102529.
- 23. Park J, Lee J, Lee J, Lee SK, Park JY. Strategies for rapid reconstruction in 3D MRI with radial data acquisition: 3D fast Fourier transform vs two-step 2D filtered back-projection. *Sci Rep.* 2020;10(1):13813.
- Mueller PR, Stark DD, Simeone JF, et al. MR-guided aspiration biopsy: needle design and clinical trials. *Radiology*. 1986;161(3):605-609.
- Sorensen TS, Schaeffter T, Noe KO, Hansen MS. Accelerating the nonequispaced fast Fourier transform on commodity graphics hardware. *IEEE Trans Med Imaging*, 2008;27(4):538-547.
- Payer C, Štern D, Bischof H, Urschler M. Regressing heatmaps for multiple landmark localization using CNNs. In: Ourselin S, Joskowicz L, Sabuncu MR, Unal G, Wells W, eds. Lecture Notes in Computer Science, vol. 9901. Springer International Publishing; 2016:230-238.

- Zhou W, Li X, Zabihollahy F, Lu DS, Wu HH. Deep learning-based automatic pipeline for 3D needle localization on intra-procedural 3D MRI. *Int J Comput Assist Radiol Surg.* 2024. Published online.
- Liu R, Lehman J, Molino P, et al. An intriguing failing of convolutional neural networks and the CoordConv Solution. Advances in Neural Information Processing Systems. 2018;31. NeurIPS 2018.
- Dosovitskiy A, Beyer L, Kolesnikov A, et al. An image is worth 16×16 words: transformers for image recognition at scale. The Ninth International Conference on Learning Representations (ICLR 2021); 2020.

SUPPORTING INFORMATION

Additional supporting information can be found online in the Supporting Information section at the end of this article.

How to cite this article: Faust JF, Krafft AJ, Polak D, et al. Rapid CNN-based needle localization for automatic slice alignment in MR-guided interventions using 3D undersampled radial white-marker imaging. *Med Phys*. 2024;51:8018–8033.

https://doi.org/10.1002/mp.17376